

Field-controlled domain wall pinning-depinning effects in a ferromagnetic nanowire-nanoislands system

V. L. Mironov,^{*} O. L. Ermolaeva, E. V. Skorohodov, and A. Yu. Klimov*Institute for Physics of Microstructures, RAS, 603950, Nizhniy Novgorod, GSP-105, Russia*

(Received 16 December 2011; revised manuscript received 30 March 2012; published 23 April 2012)

We present the results of micromagnetic modeling and experimental investigations of field-driven domain wall pinning-depinning effects in a planar system consisting of a ferromagnetic nanowire and two ferromagnetic single-domain nanoislands (NIs). It was demonstrated that the magnitude of the depinning field strongly depends on the spatial configuration of magnetic moments in the NI subsystem. An algorithm for the external magnetic field commutation and independent switching of the NI moments that permits the realization of logical operations is discussed.

DOI: [10.1103/PhysRevB.85.144418](https://doi.org/10.1103/PhysRevB.85.144418)

PACS number(s): 75.60.Ch, 75.75.Cd

I. INTRODUCTION

The field-driven motion and pinning of domain walls in ferromagnetic nanowires (NWs) are the subjects of intensive research motivated by promising applications for the development of magnetic logic and data storage systems.¹⁻⁴ The information in these devices is encoded as a direction of the local magnetic moment in the NW and write-erase or calculating processes are connected with domain reorientation accompanied by domain wall (DW) nucleation, motion, and annihilation. One of the main parameters limiting the operation rate of such systems is the velocity of DW propagation. This parameter is strongly dependent on the transverse field magnitude, DW structure, and NW shape and dimensions.⁵⁻¹⁰ In practice the DW velocity reaches a value up to 1 km/s.^{10,11} On the other hand, the operation of DW-based magnetic logical cells and data storage systems requires controlled DW pinning for preservation from accidental data erasure and to save the results of intermediate calculations. The simple method of DW pinning uses geometrical features in the NW topology and artificially patterned traps at the NW edge.¹²⁻¹⁷ The nondestructive method of DW pinning based on magnetostatic interaction of a DW with a ferromagnetic nanobar (NB) has been discussed in Refs. 18 and 19. It was shown that a tunable system of NBs located on one side of the NW allows one to control the NB-DW interaction and in particular to realize asymmetric interaction potentials. A combination of a trap and a nanobar was used recently for controllable DW pinning in nanoconstriction.²⁰ In this case the NB was located perpendicular to the NW in the vicinity of a notch. It has been demonstrated that the NB stray field substantially modifies the value of the pinning energy, depending on the relative orientation of the DW and NB magnetic moments.

In this paper we propose a different idea of DW pinning control based on the effective change of the stray field configuration in a system of two single-domain ferromagnetic nanoislands. We consider a combined system consisting of a planar ferromagnetic NW and two elongated ferromagnetic NIs placed perpendicularly on either side of the NW. The results of micromagnetic modeling and experimental magnetic force microscopy investigations of DW pinning-depinning effects depending on the spatial configuration of the magnetization in the NI subsystem are discussed. In addition,

we propose a prototype logical cell based on considered the NW-NI system and discuss an algorithm of external magnetic field commutation and independent switching of NI moments that permits the realization of logical operations.

II. THEORETICAL CONSIDERATION AND MICROMAGNETIC SIMULATIONS

We investigated the magnetization reversal processes in a polycrystalline Co₆₀Fe₄₀ planar NW-NI system, which consists of a nanowire with a special circular part (*N*) at one end and two NIs placed one on either side of the NW (see Fig. 1). The low-coercive circular pad *N* is used for the nucleation of domains with opposite orientations in an external magnetic field,²¹⁻²⁴ while the NIs are used as a magnetic gate for the field-controlled DW pinning and depinning.

To study the features of the pinning-depinning effects in the NW-NI system we performed computer micromagnetic simulations using the standard object oriented micromagnetic framework (OOMMF) code.²⁵ We considered a system with the following parameters: NW and NI thickness was 20 nm; the NW width was 100 nm, and the NW length was 3 μm; the pad diameter was 200 nm; the lateral sizes of rectangular NIs were 100 × 200 nm; the NI-NW separation was 100 nm. The geometrical sizes of the NW-NI system were chosen close to those of the experimental structure described below. The calculations were carried out for the following CoFe parameters: the exchange stiffness was $A = 3 \times 10^{-11}$ J/m, the saturation magnetization was $M_S = 1.9 \times 10^6$ A/m, and the damping constant was 0.5.²⁶ We omitted magnetocrystalline anisotropy, assuming a polycrystalline structure of our samples. In model calculations the NW-NI system was discretized into rectangular parallelepipeds with a square base of size $\delta = 2$ nm in the x, y plane and height $h = 20$ nm.

The preliminary simulations showed that the coercive field (in the x direction) for the NW without pad, H_{NW} , was 80 mT; the DW nucleating field for the NW with pad, H_{nuc} , was 35 mT; the NI saturating field in the x direction was $H_{NI}^x = 140$ mT; the NI coercive field in the y direction was $H_{NI}^y = 86$ mT (the steps of the simulated external field were 1 mT). Note that the NIs' coercive field along the x direction is much larger than the NW's coercive field, $H_{NI}^x > H_{NW}$.

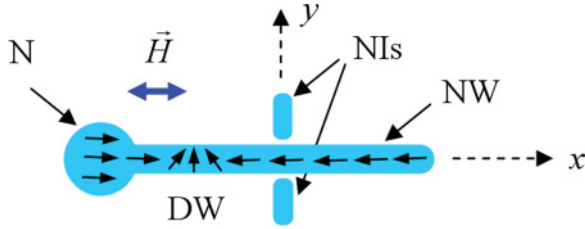


FIG. 1. (Color online) Schematic drawing of the field-driven NW-NI system.

We performed micromagnetic simulations of pinning-depinning processes in the NW-NI system. The computer experiment had the following scenario. At the first stage, the NW was magnetized uniformly (from right to left, $-x$ direction) in an external magnetic field H_{ex} , with $H_{NI}^x > H_{ex} > H_{NW}$. Afterward we applied the reversed field (from left to right, $+x$ direction) $H_{NW} > H_{ex} > H_{nuc}$. In this case, reorientation of the magnetization in the circular pad and transverse DW formation were observed. The result of micromagnetic simulation of the DW in the NW is represented in Fig. 2. It is seen that the DW had the characteristic trapezoidal structure.

The process of NW magnetization reversal is accompanied by DW propagation from the pad to the free NW end and can be stopped due to magnetostatic interaction with the NI gates. To estimate the pinning energy and depinning fields for different configurations of magnetization in the NW-NI system, we considered the dependence of the DW-NI interaction energy on DW position. In general, the potential energy of the NW in an external magnetic field can be calculated as follows:

$$E_{NW}(x_{DW}) = - \int_{V_{NW}} (\vec{M}_{NW} \cdot \vec{H}) dV_{NW}, \quad (1)$$

where $\vec{M}_{NW}(\vec{r})$ is the magnetization distribution in the NW; \vec{H} is the sum of magnetic stray fields from the NIs and the uniform external magnetic field, $\vec{H} = \vec{H}_{NI} + \vec{H}_{ex}$; x_{DW} is the position of the DW center; the integration is performed over the NW volume. The nanoislands' stray magnetic field can be presented in the following form:

$$\vec{H}_{NI}(\vec{r}) = \int_{V_{NI}} \left(\frac{3[\vec{M}_{NI}(\vec{r}_{NI}) \cdot (\vec{r} - \vec{r}_{NI})]}{|\vec{r} - \vec{r}_{NI}|^5} (\vec{r} - \vec{r}_{NI}) - \frac{\vec{M}_{NI}(\vec{r}_{NI})}{|\vec{r} - \vec{r}_{NI}|^3} \right) dV_{NI}, \quad (2)$$

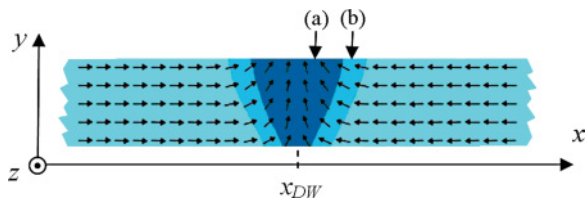


FIG. 2. (Color online) The simulated DW structure in a CoFe NW. (A small part of size $500 \times 100 \text{ nm}^2$ is presented.) The magnetization vectors in the region (a) are turned at the angles $\alpha_a \geq 0.5 \pi/2$ and in the region (b) at $0.1 \pi/2 \leq \alpha_b \leq 0.5 \pi/2$. The regions (a) and (b) are marked by dark tones.

where the integration is performed over the nanoisland volume V_{NI} ; \vec{r}_{NI} is the radius vector with coordinates x_{NI} , y_{NI} , and z_{NI} , which are the coordinates of integration. Substituting the $\vec{M}_{NI}(\vec{r})$ distribution from the OOMMF simulation, one can calculate the model stray field from islands with a nonuniform magnetization distribution. In estimating calculations we supposed that the magnetization of the NW and NIs does not depend on the z coordinate.

The dependence of the interaction energy E_{NW} on DW position allows one to estimate the pinning energy and depinning fields for different configurations of magnetization in the NW-NI system. We carried out numerical calculations of the energy landscape based on formulas (1) and (2) and the model of a rigid DW, omitting the changing of exchange and demagnetizing energy with DW propagation from the pad to the free NW end.^{20,27} The simulated NI magnetization \vec{M}_{NI} and DW distribution \vec{M}_{NW} (Fig. 2) were used in the model $E_{NW}(x_{DW})$ calculations.

The effects of DW pinning depend on the mutual configuration of magnetization in the NW and NIs. Different possible variants of NW and NI magnetization, the corresponding dependences of the NW-NI system energy on the DW position and the results of micromagnetic modeling are presented in Figs. 3–6.

Let us analyze first the configuration represented in Fig. 3(a) (A-type configuration). In this case the magnetization vectors in the NW and in NIs are directed toward each other (head-to-head or tail-to-tail configuration). The corresponding dependences of energy $E_{NW}(x_{DW})$ calculated on the base of the rigid DW model for different external fields are presented in Fig. 3(b). The DW propagation is connected with overcoming the energy barrier, which is defined mainly by the magnetostatic interaction of the quasiuniform NW magnetization outside the DW with the x component of the NI field. Note that the magnitude of the barrier is independent of the DW direction due to the symmetry of the NIs' magnetic configuration. Hence, in a weak magnetic field the DW will be pinned in the region before the NI gate. The estimate of the energy barrier at zero field is $E_B = 508 \text{ eV}$. In an external magnetic field the pinning barrier is decreased and at 47 mT (depinning field H_B) it vanishes completely [curve 2 in Fig. 3(b)]. We performed also accurate micromagnetic calculations of the energy landscape $E_{NW}(x_{DW})$, taking into account the effects of the DW and NIs magnetization disturbance. For this purpose in the model experiment we considered the step-by-step motion of the DW along the NW in an external magnetic field equal to the depinning field, $H_{ex} = H_B$. At each k th step we registered the DW position x_{DW}^k and corresponding magnetization distributions $\vec{M}_{NW}^k(\vec{r})$ in the nanowire and $\vec{M}_{NI}^k(\vec{r})$ in nanoislands. It allowed us to calculate numerically the NI stray field distribution by the formula (2) and then calculate the interaction energy $E_{NW}^k(x_{DW}^k)$ by the formula (1). The results of these calculations are presented as circles in Fig. 3(b). The comparisons show that the relative error in the energy landscape calculations based on the rigid DW model is less than 5% and can be neglected in qualitative considerations. The critical depinning field estimated directly from OOMMF modeling was $H_B = 49 \text{ mT}$ (in simulations the field increase step was 1 mT). The micromagnetic simulations also confirmed the DW pinning before the NI gate. The position

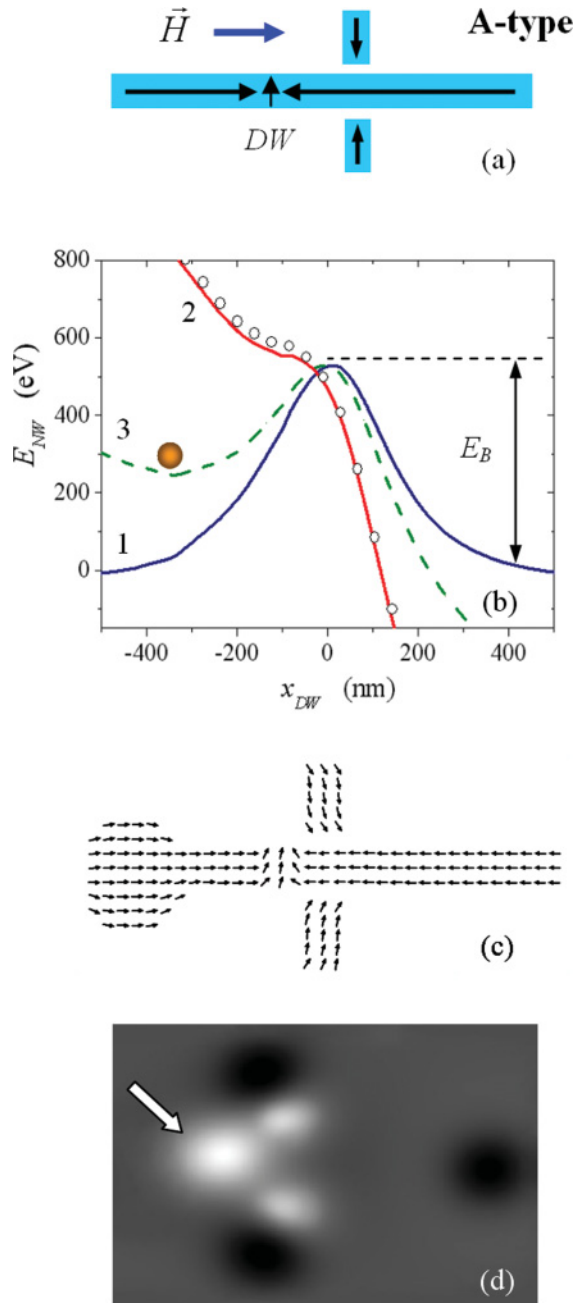


FIG. 3. (Color online) (a) The A-type configuration of magnetization in the NW-NI system in an external magnetic field. (b) The potential energy profiles $E_{NW}(x_{DW})$ for different external magnetic fields. The solid line 1 is the energy profile at zero field. The solid line 2 is for the critical external field $H_B = 47$ mT. The dashed line 3 is for the intermediate field $0.5H_B$. The DW pinning position is indicated schematically by the circle on curve 3. The energy landscape calculated directly from OOMMF simulations taking into account the effects of DW and NI magnetization disturbance is indicated by circles. (c) The model magnetization distribution in the NW-NI system at $H_{ex} = H_{nuc}$, demonstrating the DW pinning on the potential barrier before the NIs. The S state in the NIs' magnetization was caused by the external magnetic field. (d) The model MFM contrast distribution from the NW-NI system (without nucleating pad) corresponding to the magnetization distribution shown in (c). The white arrow in the MFM image indicates the bright pole, which corresponds to a transverse DW.

of the pinned DW in the external magnetic field $H_{ex} = H_{nuc}$ is shown in Fig. 3(c).

In addition, we calculated the expected magnetic force microscopy (MFM) contrast distributions for the configuration of magnetization presented in Fig. 3(c) to compare with results of experimental MFM investigations. We considered a widely used MFM method, called phase contrast imaging. In this regime the MFM signal is registered as the phase shift $\Delta\varphi$ of cantilever oscillations under the magnetostatic interaction between tip and sample. In a model of a linear oscillator with point mass, this value is proportional to the z component of the magnetic force gradient:²⁸⁻³⁰

$$\Delta\varphi = -\frac{Q}{K} \frac{\partial F_z}{\partial z}, \quad (3)$$

where Q is the cantilever quality factor, K is the cantilever force constant, and F_z is the z component of the magnetic force. In the point probe approximation this value is proportional to the second derivative of the sample's magnetic stray field, $\partial^2 H_z / \partial z^2$. The normalized model MFM contrast can be calculated based on the model magnetization distribution \vec{M}_{ij} obtained from OOMMF simulations. Indeed, the z component of the magnetic field from the \vec{M}_{ij} point dipole can be written in the following form:

$$H_z^{ij}(x, y, z) = \frac{3z(\vec{M}_{ij} \cdot \vec{r}_{ij})}{r_{ij}^5} - \frac{(\vec{M}_{ij})_z}{r_{ij}^3}, \quad (4)$$

where \vec{r}_{ij} is the radius vector from the elementary dipole \vec{M}_{ij} to the point of observation; r_{ij} is the modulus of \vec{r}_{ij} . Then the normalized MFM contrast distribution is calculated as

$$\Delta\varphi(x, y) = -\frac{\partial^2}{\partial z^2} \sum_{ij} H_z^{ij}(x, y, z) \Big|_{z=z_0}, \quad (5)$$

where z_0 is the scanning height.

The model MFM image corresponding to the model magnetization distribution [Fig. 3(c)] is presented in Fig. 3(d). The calculations were performed for the scanning height of 50 nm (close to experimental conditions). The DW is seen as the bright pole located before the NI poles [it is indicated by the arrow in Fig. 3(d)].

In the B -type configuration represented in Fig. 4(a) we have head-to-head (tail-to-tail) magnetization in the NW but tail-to-tail (head-to-head) magnetization in the NIs. The energy profile $E_{NW}(x_{DW})$ has a potential well [Fig. 4(b)] and the DW is pinned at the region directly between the NIs. Thus, the NW remagnetization is connected with DW escape from the energy well. The value of the energy well is defined mainly by the magnetostatic interaction of the NW magnetization outside the DW with the x component of the NI field and does not depend on DW direction. The estimate of the activation energy E_W at zero field is 508 eV. In an external magnetic field the pinning barrier connected with the potential well is decreased [see curve 3 in Fig. 4(b)] and at 47 mT (depinning field H_W) it vanishes completely [curve 2 in Fig. 4(b)].

The micromagnetic modeling confirmed the DW pinning between NIs for the B -type configuration. The magnetization distribution in the NW-NI system with pinned DW is represented in Fig. 4(c). The depinning field estimated directly from the OOMMF simulations was 49 mT.

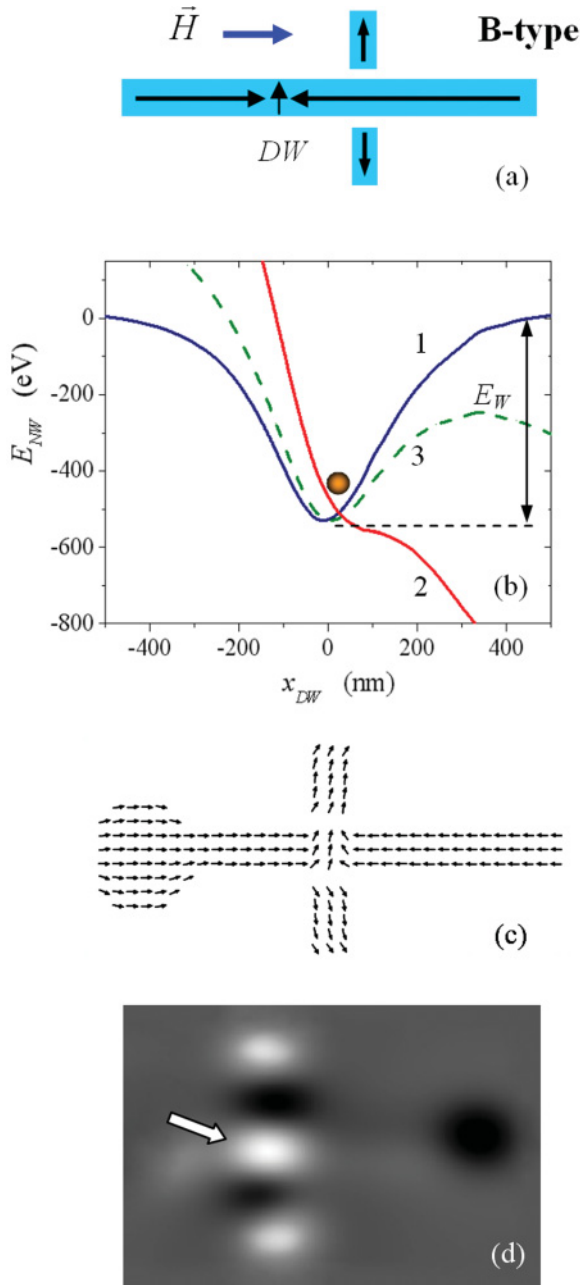


FIG. 4. (Color online) (a) The *B*-type configuration of magnetization in the NW-NI system in an external magnetic field. (b) The energy E_{NW} profile for different external magnetic fields. The solid line 1 is the energy profile at zero external field. The dot-dashed line 2 is for the critical magnetic field $H_W = 47$ mT. The dashed line 3 is for the intermediate field $0.5H_W$. The DW pinning position is indicated schematically by a circle. (c) The model magnetization distribution at $H_{ex} = H_{nuc}$, demonstrating the DW pinning in the potential well between NIs. (d) The normalized model MFM contrast distribution from the NW-NI system (without nucleating pad) corresponding to the magnetization distribution shown in (c). The white arrow in the MFM image indicates the bright pole corresponding to the transverse DW.

Figure 4(d) shows the expected MFM contrast distribution corresponding to the configuration of magnetization presented in Fig. 4(c). The DW is seen as the bright pole located between the NI poles [it is indicated by the arrow in Fig. 4(d)].

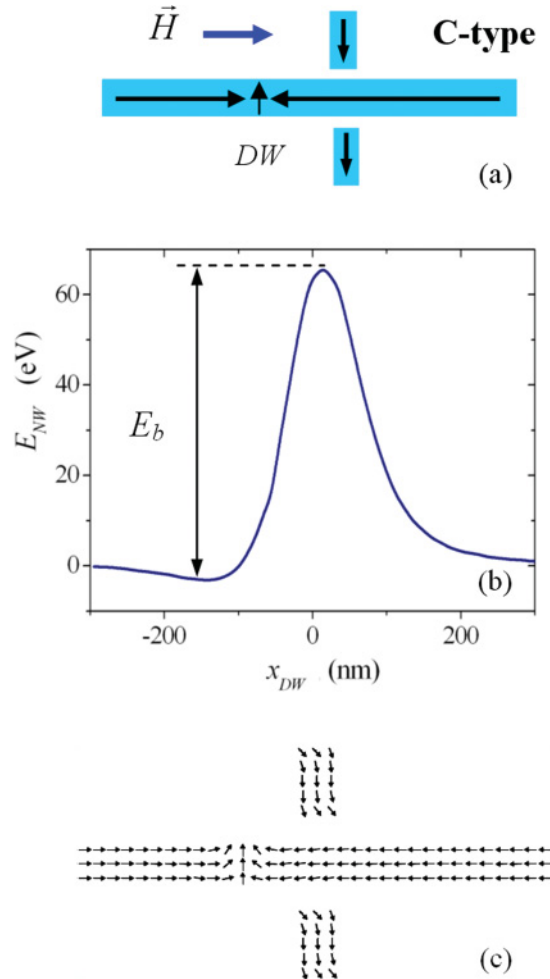


FIG. 5. (Color online) (a) The *C*-type configuration of magnetization in the NW-NI system. (b) The energy profile $E_{NW}(x_{DW})$ at zero external field. (c) The model magnetization distribution at zero external field (after applying the driving field $H_{ex} = 2.5$ mT) demonstrating the DW pinning on the potential barrier before the NIs. The *S* state in the NIs' magnetization is caused by the external magnetic field.

The third possible configuration, in which the NI moments have the same direction (head to tail) but the DW magnetization has the opposite direction (*C*-type configuration), is presented in Fig. 5(a). In this case the x components of the stray magnetic fields from the NIs are partly compensated. The calculated energy landscape has a potential barrier caused by interaction of the DW with the y component of the NI field [Fig. 5(b)]. Hence, in the *C*-type configuration a DW can be pinned in the region before the NIs. The asymmetry of the energy landscape $E_{NW}(x_{DW})$ is connected with the *S* state in the NI magnetization distribution. The model distribution of magnetization for the *C*-type configuration with pinned DW is presented in Fig. 5(c). In simulations we artificially initialized a DW in the left front of the NW and used the small driving field $H_{ex} = 2.5$ mT to stimulate DW propagation. The effect of DW pinning was registered as the stabilization of the DW position in the external magnetic field. The *C*-type configuration has a very small pinning energy in comparison

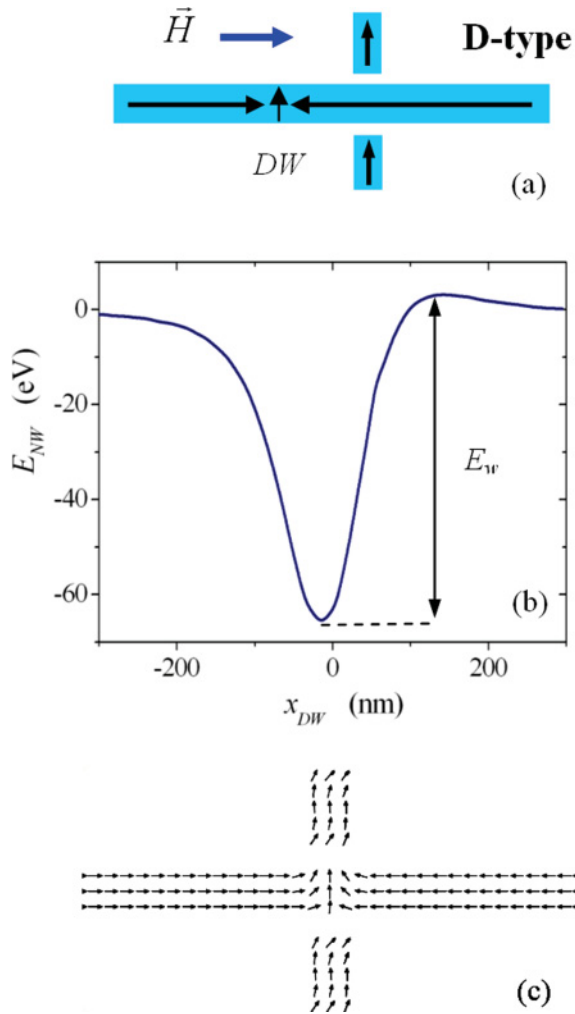


FIG. 6. (Color online) (a) The D -type configuration of magnetization in the NW-NI system. (b) The energy profile $E_{NW}(x_{DW})$ at zero external field. (c) The model magnetization distribution at zero external field (after applying $H_{ex} = 2.5$ mT) demonstrating the DW pinning in the potential well between NIs.

with the A configurations. The estimate of the energy barrier E_b at zero external field is 65 eV. The calculated depinning field (estimated as where the barrier vanishes in the external field) is 9 mT, which practically coincides with 10 mT estimated directly from the OOMMF simulations.

The fourth possible configuration (D type) is presented in Fig. 6(a). In this case the directions of magnetization in both NIs are the same (head to tail) and coincide with the DW orientation. The energy landscape $E_{NW}(x_{DW})$ has a potential well caused by interaction of the DW with the y component of the NI field [Fig. 6(b)]. The asymmetry of the energy landscape $E_{NW}(x_{DW})$ is connected with the S state in the NI magnetization distribution. Hence, in this case the DW can be pinned in the region directly between the NIs [see the position of the pinned DW in Fig. 6(c)] but this configuration has a small pinning energy in comparison with B configurations. The estimate of the energy barrier E_w at zero field is 65 eV. The depinning field estimated as the potential wall vanishing in the external field is 9 mT. The depinning

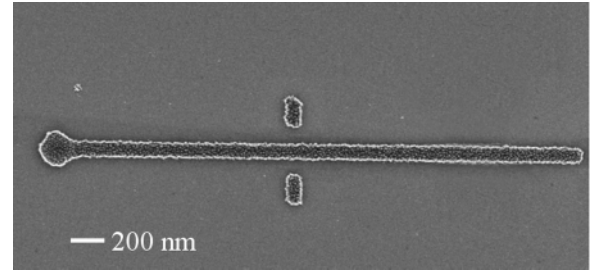


FIG. 7. SEM image of the nanowire-nanoisland system.

field estimated directly from the OOMMF simulations was 10 mT.

III. EXPERIMENT

The NW-NI systems were fabricated using negative e -beam lithography and ion etching processes. The $\text{Co}_{60}\text{Fe}_{40}$ (20 nm)/V (15 nm)/Cu (10 nm) multilayer structure was deposited onto a Si substrate by magnetron sputtering. Afterward the sample was covered by fullerene C_{60} (80 nm), which was used as e -beam resist. The initial protective mask was formed in C_{60} by exposure in the ELPHY PLUS system (based on the scanning electron microscope SUPRA 50VP) with subsequent chemical treatment in an organic solvent. Afterward, the image was transferred to the Cu layer by Ar^+ -ion etching and further to the V layer by plasma etching in Freon. At the final stage, the NW-NI system was fabricated in the ferromagnetic $\text{Co}_{60}\text{Fe}_{40}$ layer by Ar^+ -ion etching. The characteristic scanning electron microscope (SEM) image of the NW-NI system is presented in Fig. 7. The width of the NW was 100 nm, the NW length was about $2.8 \mu\text{m}$; lateral dimensions of the NIs were $100 \times 200 \text{ nm}^2$, the NI-NW separation was 100 nm; and the diameter of the nucleating part was 200 nm.

The magnetic states and the magnetization-reversal effects in the NW-NI system were studied using the vacuum multimode scanning probe microscope Solver-HV, which is equipped with a dc electromagnet incorporated in a vacuum vibration-insulating platform (the maximal magnitude of the magnetic field is 0.1 T). The scanning probes were cobalt coated with a thickness of 30 nm. Before measurements, the tips were magnetized along the symmetry axes (Z) in a 1 T external magnetic field. The magnetic force microscope measurements were performed in the noncontact constant-height mode. The phase shift $\Delta\phi$ of cantilever oscillations under the gradient of the magnetic force was registered to obtain the MFM contrast. All measurements were performed in a vacuum of 10^{-4} Torr, which improved the MFM signal due to an increase in the cantilever quality factor.

IV. RESULTS AND DISCUSSION

We investigated the dependence of the pinning-depinning processes in the NW-NI system (Fig. 7) on the configuration of magnetization in the NIs. The experiment was performed *in situ* in the MFM Solver HV vacuum chamber. First, we studied the NW magnetization reversal when the magnetic moments in the NW-NI system corresponded to the A -type config-

uration. The different stages of the NW remagnetization experiment are represented in Fig. 8. The initial state was prepared by previously magnetizing the sample along the NW (in the $-x$ direction) with $H_{\parallel} \geq 70$ mT (the approximate rate of field increase was 10 mT/s) and subsequently magnetizing the NIs in a perpendicular (in the y direction) magnetic field $H_{\perp} = 70$ mT and remagnetizing (in the $-y$ direction) in a reversed field H_{\perp} with a magnitude of about 49 mT. The head-to-head configuration is formed in the reversed field due to a small difference in the NIs' coercivity. The MFM image of the initial state is presented in Fig. 8(a). It is seen that the MFM contrast pole positions in the MFM image of the initial state correspond to the type-A configuration (the dark pole corresponds to the tail and the bright pole to the head of the magnetization vector). Afterward the external field H_{\parallel} was applied in the reversed (x) direction and the NW remagnetization effect was studied. All external field manipulations were performed with 1 mT steps. The approximate rate of change of the field was about 10 mT/s. When H_{\parallel} exceeded 30 mT (DW nucleation field H_{nuc}) we registered the appearance of an additional bright pole in the MFM image [indicated by the white arrow in Fig. 8(b)] corresponding to the DW [compare with Fig. 3(d)]. So we observed the DW pinning on the potential barrier before the NIs. The DW position was stable in external magnetic fields up to $H_{\parallel} = 56$ mT, but when H_{\parallel} exceeded 56 mT (DW depinning field H_B) the remagnetization of the NW was observed [see the change of the MFM contrast at the free NW end in Fig. 8(c)].

A different situation was observed for the magnetization reversal experiment in the B -type configuration of the NW-NI magnetic moments. The initial state was prepared by an analogous method to that for the A -type configuration but for the generation of the tail-to-tail configuration in the NIs we used the inverse procedure of NI remagnetization in a perpendicular magnetic field. The different stages of the NW remagnetization experiment are demonstrated in Fig. 9. The MFM image of the initial state is presented in Fig. 9(a). The MFM pole positions confirm the B -type configuration. Analogously, when the external magnetic field H_{\parallel} (x direction) exceeded 30 mT, we registered the appearance of an additional bright MFM pole [indicated by the white arrow in Fig. 9(b)] corresponding to the DW. But it is seen that in this case the DW was pinned right in between the NIs. We believe that it can be explained as DW pinning in a potential well [compare with Fig. 4(d)]. The depinning field was practically the same as in the case of the A -type configuration, so when H_{\parallel} exceeded 56 mT (DW depinning field H_W) we observed the remagnetization of the NW, which was registered as a changing of the MFM contrast at the free NW end [see Fig. 9(c)]. The similarity between the magnitudes of the depinning fields H_B and H_W in the A - and B -type configurations observed in model simulations as in experimental measurements allows one to suggest that the magnetostatic DW-NI interaction in such systems is quite weak and the rigid DW approximation is valid in this case

The results of NW magnetization reversal in a NW-NI system with C - or D -type configuration are presented in Fig. 10. The initial state was prepared by previous magnetization along the NW ($-x$) and subsequent NI remagnetization

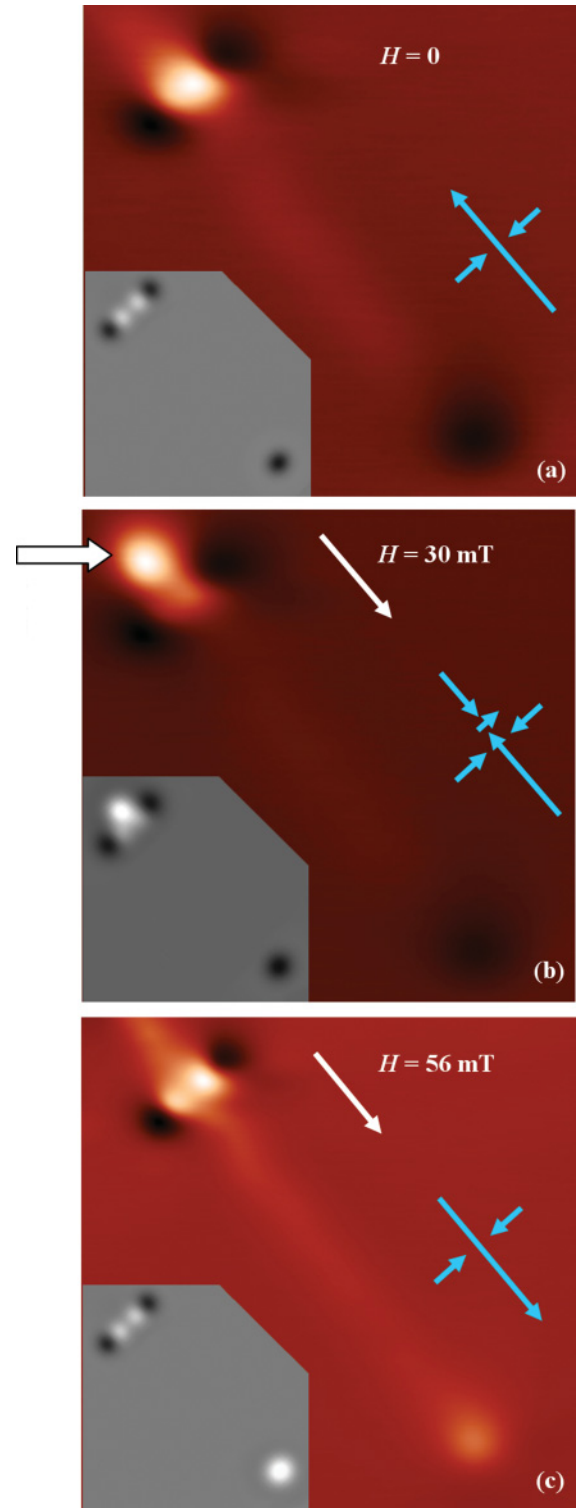


FIG. 8. (Color online) MFM images of the NW-NI system after the application of an external magnetic field. (a) Initial state with A -type configuration after previous magnetization. (b) MFM image of DW pinned at the barrier near the NIs after applying 30 mT external field (the DW position is indicated by the white arrow). (c) MFM image of the NW-NI system after remagnetization in 56 mT external magnetic field. The arrows at the right side of the pictures show the configuration schemes of the magnetization. The corresponding model MFM images are shown as insets in the lower left corners of the pictures.

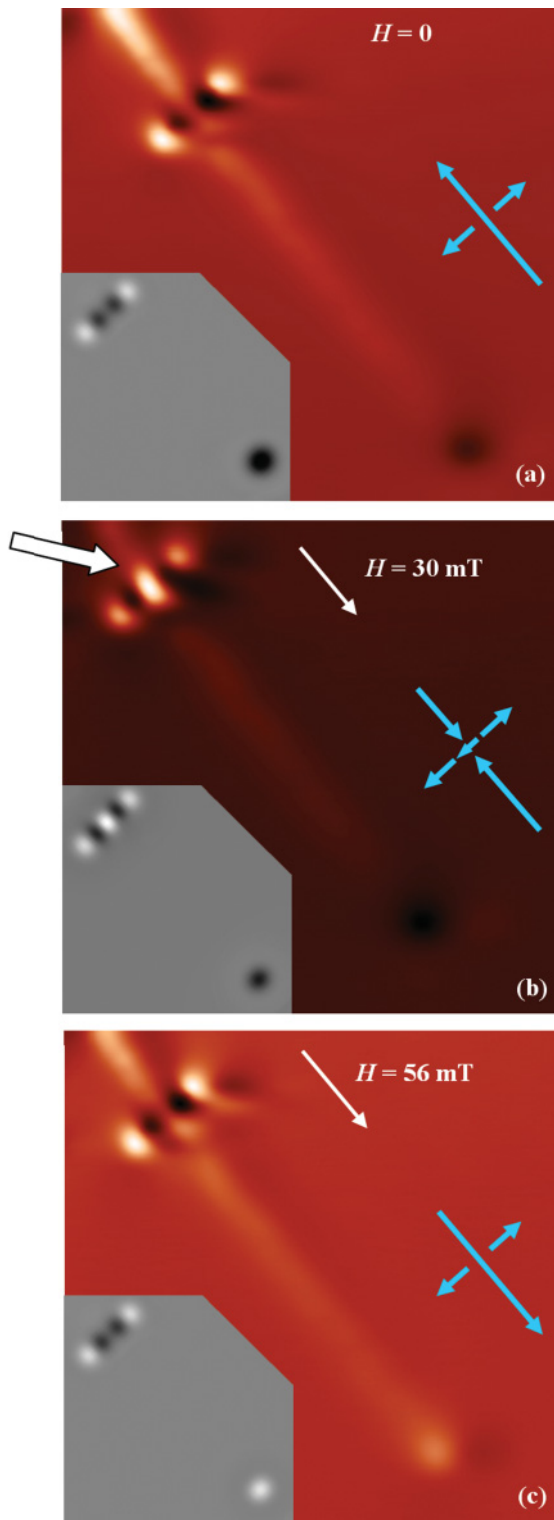


FIG. 9. (Color online) MFM images of the NW-NI system after the application of an external magnetic field. (a) Initial state with *B*-type configuration after previous magnetization. (b) MFM image of DW pinned at the well between NIs after applying 30 mT external field (the DW position is indicated by the white arrow). (c) MFM image of the NW-NI system after remagnetization in 56 mT external magnetic field. The arrows at the right side of the pictures show the configuration schemes of the magnetization. The corresponding model MFM images are shown as insets in the lower left corners of the pictures.

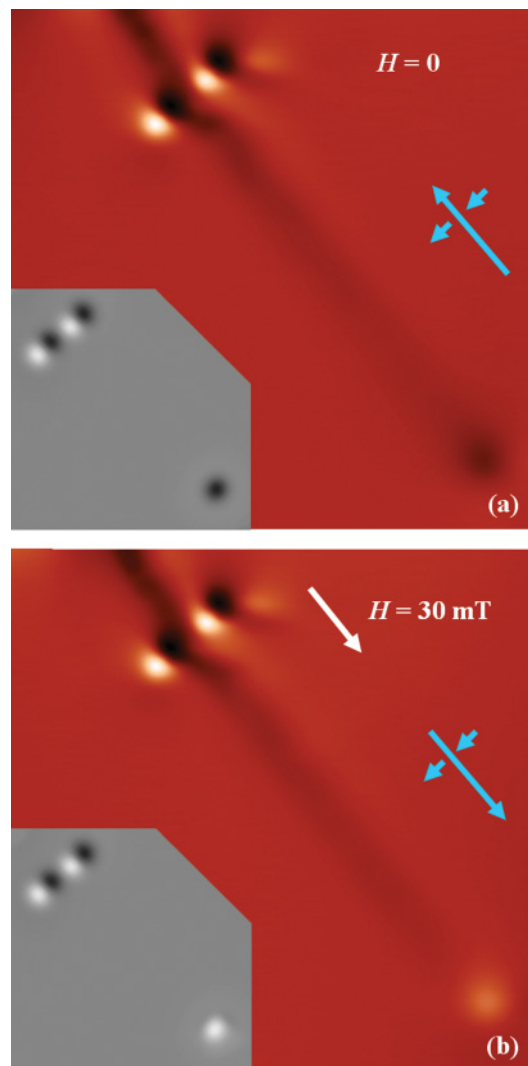


FIG. 10. (Color online) MFM images of magnetization reversal of the NW-NI system with *C*- or *D*-type configuration in an external magnetic field. (a) Initial state after previous magnetization. (b) MFM image of the NW-NI system after applying 30 mT external field. DW pinning was not observed because for this system the pinning field was much less than the nucleating field. The arrows at the right side of the pictures show the configuration schemes of the magnetization. The corresponding model MFM images are shown as insets in the lower left corners of the pictures.

in a perpendicular magnetic field ($-y$) with a magnitude of 70 mT exceeding the NIs' coercivity. Subsequently a reversed external magnetic field H_{\parallel} was applied and the process of remagnetization was studied. In this case we did not register the pinning of the DW since the remagnetization effect was observed just after applying the nucleating external magnetic field $H_{\parallel} = H_{\text{nuc}} = 30$ mT. This fact demonstrates that for our NW-NI system the DW nucleation field is larger than the depinning field connected with the DW-NI interaction in the *C*- or *D*-type configuration ($H_{\text{nuc}} > H_b, H_w$).

As is seen, the experimental results are in qualitative accordance with the previous theoretical estimations and micromagnetic modeling. However, there are considerable

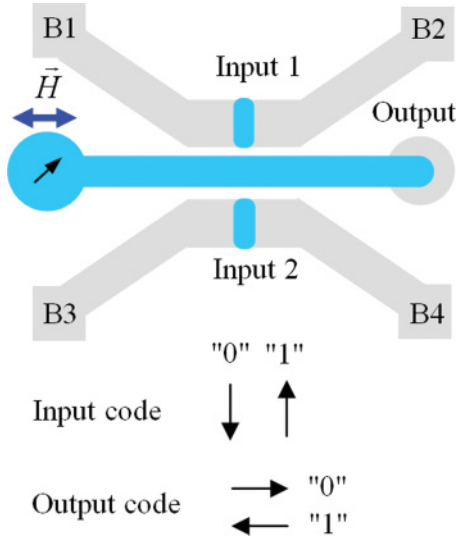


FIG. 11. (Color online) Drawing of the schematic NW-NI logical cell and the coding of the input-output states.

quantitative differences in the estimations of the fields H_{nuc} , H_B , and H_W . We believe that the high values of the depinning fields observed in the experiments are connected with NW edge roughness. As estimated from SEM images, the rms edge roughness for our NW-NI system was about 8 nm (8% of the width). Direct OOMMF simulations taking into account the estimated edge roughness have demonstrated a considerable increase of the depinning field close to the experimentally observed value.

The NW-NI system described above can be considered as a prototype of a magnetic logical cell (MLC), which realizes the “exclusive disjunction” logical operation (so-called XOR). For example, the input signals can be encoded as the direction of the magnetic moment in the NIs and the output information as the moment direction at the free end of the NW. Figure 11 shows a scheme of inputs-outputs and possible input-output information coding.

The algorithm for the MLC operation includes a periodic reactivation cycle and a logical computing cycle consisting of input information and writing and reading of the result of the logical operation. The logical calculations can be organized as follows. The first stage is the initialization process when the logical “1” is written in the NW by an external magnetic field H_{\parallel} ($H_{\parallel} > H_B, H_W$) applied in the $-x$ direction. Afterward the input information is written in the NIs by local magnetic fields, which can be created for instance, with current buses B1, B2 and B3, B4 (see Fig. 11). At the final stage the reversed external magnetic field H_{\parallel} with amplitude $H_B, H_W > H_{\parallel} > H_{\text{nuc}}$ ($H_{\text{nuc}} > H_b, H_w$) is applied in the x direction and the output information is read. The magnetic state of the NW free end can be analyzed using the local magneto-optical Kerr

TABLE I. The logical output states for all input states (truth table).

Input 1	Input 2	Output
0	0	0
0	1	1
1	0	1
1	1	0

effect or by means of tunneling magnetoresistance. Afterward the cycle of operation is repeated. The correspondence between input and output information in such a MLC is represented in Table I.

V. SUMMARY

Thus, we investigated the DW pinning-depinning effects in a hybrid system consisting of a ferromagnetic NW (with a circular pad at one end) and a two-NI gate placed perpendicularly at the middle part of NW. Micromagnetic simulations and direct magnetic force microscopy measurements have shown that in dependence on the relative orientation of the magnetic moments in the NW and NI subsystem there are two variants of DW pinning connected with a potential barrier (*A*-type configuration) or a potential well (*B*-type configuration) caused by magnetostatic interaction between the DW magnetization structure in the NW and local NI stray fields.

For the $\text{Co}_{60}\text{Fe}_{40}$ -based NW-NI system consisting of a $100 \times 2800 \times 20 \text{ nm}^3$ nanowire with a nucleating part 200 nm in diameter and a $200 \times 100 \times 20 \text{ nm}^3$ nanoisland gate (with 100 nm NW-NI separation), the nucleating field 30 mT and depinning field 56 mT in *A*- and *B*-type configurations were registered. When the magnetic moments of the NIs were set in *C*- or *D*-type configurations, the DW pinning effects were not observed at all.

Potentially different combinations of NWs with independently switched NIs are very promising for the development of new types of magnetic logic cells and other DW-based computing systems.

ACKNOWLEDGMENTS

The authors are very thankful to S. A. Gusev, S. N. Vdovichev, and V. V. Rogov for assistance in sample preparation and to B. A. Gribkov and A. A. Fraerman for very fruitful discussions. We are grateful to J. A. Blackman (University of Reading, UK) for useful discussions and suggestions. We also thank the referees for very helpful comments. This work was supported by the Russian Foundation for Basic Research (Projects No. 11-02-00434 and No. 11-02-00589). E.V.S wishes to thank the Carl Zeiss Company for financial support.

*mironov@ipm.sci-nnov.ru

¹D. A. Allwood, G. Xiong, M. D. Cooke, C. C. Faulkner, D. Atkinson, N. Vernier, and R. P. Cowburn, *Science* **296**, 2003 (2002).

²D. A. Allwood, G. Xiong, C. C. Faulkner, D. Atkinson, D. Petit, and R. P. Cowburn, *Science* **309**, 1688 (2005).

³L. O’Brien, D. E. Read, H. T. Zeng, E. R. Lewis, D. Petit, and R. P. Cowburn, *Appl. Phys. Lett.* **95**, 232502 (2009).

- ⁴H. T. Zeng, D. E. Read, L. O'Brien, J. Sampaio, E. R. Lewis, D. Petit, and R. P. Cowburn, *Appl. Phys. Lett.* **96**, 262510 (2010).
- ⁵T. Ono, H. Miyajima, K. Shigeto, K. Mibu, N. Hosoi, and T. Shinjo, *Science* **284**, 468 (1999).
- ⁶M. T. Bryan, T. Schrefl, D. Atkinson, and D. A. Allwood, *J. Appl. Phys.* **103**, 073906 (2008).
- ⁷A. Kunz and S. C. Reiff, *J. Appl. Phys.* **103**, 07D903 (2008).
- ⁸G. S. D. Beach, C. Nistor, C. Knutson, M. Tsoi, and J. L. Erskine, *Nat. Mater.* **4**, 741 (2005).
- ⁹K. Weerts, P. Neutens, L. Lagae, and G. Borghs, *J. Appl. Phys.* **103**, 094307 (2008).
- ¹⁰S. Glathe, I. Berkov, T. Mikolajick, and R. Mattheis, *Appl. Phys. Lett.* **93**, 162505 (2008).
- ¹¹D. Atkinson, D. A. Allwood, G. Xiong, M. D. Cooke, C. C. Faulkner, and R. P. Cowburn, *Nat. Mater.* **2**, 85 (2003).
- ¹²X. Zhu, D. A. Allwood, G. Xiong, R. P. Cowburn, and P. Grütter, *Appl. Phys. Lett.* **87**, 062503 (2005).
- ¹³E. R. Lewis, D. Petit, L. Thevenard, A. V. Jausovec, L. O'Brien, D. E. Read, and R. P. Cowburn, *Appl. Phys. Lett.* **95**, 152505 (2009).
- ¹⁴D. Petit, A. V. Jausovec, D. E. Read, and R. P. Cowburn, *J. Appl. Phys.* **103**, 114307 (2008).
- ¹⁵D. Petit, A. V. Jausovec, H. T. Zeng, E. R. Lewis, L. O'Brien, D. E. Read, and R. P. Cowburn, *Phys. Rev. B* **79**, 214405 (2009).
- ¹⁶K. O'Shea, S. McVitie, J. N. Chapman, and J. M. R. Weaver, *Appl. Phys. Lett.* **93**, 202505 (2008).
- ¹⁷L. K. Bogart, D. Atkinson, K. O'Shea, D. McGrouther, and S. McVitie, *Phys. Rev. B* **79**, 054414 (2009).
- ¹⁸H. T. Zeng, D. Petit, L. O'Brien, D. Read, E. R. Lewis, and R. P. Cowburn, *J. Magn. Magn. Mater.* **322**, 2010 (2010).
- ¹⁹L. O'Brien, D. Petit, E. R. Lewis, R. P. Cowburn, D. E. Read, J. Sampaio, H. T. Zeng, and A.-V. Jausovec, *Phys. Rev. Lett.* **106**, 087204 (2011).
- ²⁰S. M. Ahn, K. W. Moon, C. G. Cho, and S. B. Choe, *Nanotechnology* **22**, 085201 (2011).
- ²¹D. A. Allwood, G. Xiong, and R. P. Cowburn, *J. Appl. Phys.* **100**, 123908 (2006).
- ²²A. Kunz and S. C. Reiff, *Appl. Phys. Lett.* **94**, 192504 (2009).
- ²³S. Glathe, M. Zeisberger, R. Mattheis, and D. Hesse, *Appl. Phys. Lett.* **97**, 112508 (2010).
- ²⁴V. L. Mironov, O. L. Ermolaeva, S. A. Gusev, A. Yu. Klimov, V. V. Rogov, B. A. Gribkov, O. G. Udalov, A. A. Fraerman, R. Marsh, C. Checkley, R. Shaikhaidarov, and V. T. Petrashov, *Phys. Rev. B* **81**, 094436 (2010).
- ²⁵M. J. Donahue and D. G. Porter, Interagency Report No. NISTIR 6376, National Institute of Standards and Technology, Gaithersburg, [<http://math.nist.gov/oommf>].
- ²⁶V. Satya Narayana Murthy, C. Krishnamoorthi, R. Mahendiran, and A. O. Adeyeye, *J. Appl. Phys.* **105**, 023916 (2009).
- ²⁷L. O'Brien, D. Petit, H. T. Zeng, E. R. Lewis, J. Sampaio, A. V. Jausovec, D. E. Read, and R. P. Cowburn, *Phys. Rev. Lett.* **103**, 077206 (2009).
- ²⁸D. Rugar, H. J. Mamin, P. Guethner, S. E. Lambert, J. E. Stern, I. McFadyen, and T. Yogi, *J. Appl. Phys.* **68**, 1169 (1990).
- ²⁹R. D. Gomez, E. R. Burke, and I. D. Mayergoyz, *J. Appl. Phys.* **79**, 6441 (1996).
- ³⁰A. Thiaville, J. Miltat, and J. M. Garcia, in *Magnetic Microscopy of Nanostructures*, edited by H. Hopster and H. P. Oepen (Springer-Verlag, Berlin, 2005).